How DNA Polymerase X Preferentially Accommodates Incoming dATP Opposite 8-Oxoguanine on the Template

Benedetta Sampoli Benítez,[†*] Zachary R. Barbati,[†] Karunesh Arora,[‡] Jasmina Bogdanovic,[†] and Tamar Schlick[§*]
[†]Department of Natural Sciences, Marymount Manhattan College, New York, New York; [‡]Department of Chemistry, University of Michigan, Ann Arbor, Michigan; and [§]Department of Chemistry and Courant Institute of Mathematical Sciences, New York University, New York, New York

ABSTRACT The modified base 8-oxo-7,8-dihydro-2′-deoxyguanosine (oxoG) is a common DNA adduct produced by the oxidation of DNA by reactive oxygen species. Kinetic data reveal that DNA polymerase X (pol X) from the African swine fever virus incorporates adenine (dATP) opposite to oxoG with higher efficiency than the non-damaged G:C basepair. To help interpret the kinetic data, we perform molecular dynamics simulations of pol X/DNA complexes, in which the template base opposite to the incoming dNTP (dCTP, dATP, dGTP) is oxoG. Our results suggest that pol X accommodates the oxoG$_{syn}$:A mispair by sampling closed active conformations that mirror those observed in traditional Watson-Crick complexes. Moreover, for both the oxoG$_{syn}$:A and oxoG:C ternary complexes, conformational sampling of the polymerase follows previously described large subdomain movements, local residue motions, and active site reorganization. Interestingly, the oxoG$_{syn}$:A system exhibits superior active site geometry in comparison to the oxoG:C system. Simulations for the other mismatch basepair complexes reveal large protein subdomain movement for all systems, except for oxoG:G, which samples conformations close to the open state. In addition, active site geometry and basepairing of the template base with the incoming nucleotide, reveal distortions and misalignments that range from moderate (i.e., oxoG:A$_{syn}$) to extreme (i.e., oxoG$_{anti/syn}$:G). These results agree with the available kinetic data for pol X and provide structural insights regarding the mechanism by which this polymerase can accommodate incoming nucleotides opposite oxoG. Our simulations also support the notion that α-helix E is involved both in DNA binding and active site stabilization. Our proposed mechanism by which pol X can preferentially accommodate dATP opposite template oxoG further underscores the role that enzyme dynamics and conformational sampling operate in polymerase fidelity and function.

INTRODUCTION

DNA damage is caused by a plethora of exogenous and endogenous factors, many of which may alter the chemistry of nucleotide bases (1,2). Repair systems are thus critical for maintaining the integrity of native DNA. The oxidative lesion 8-oxo-7,8-dihydro-2′-deoxyguanosine (oxoG) is a common DNA adduct that has a high mutagenic potential (3,4). The damage occurs when electrophilic oxidants (reactive oxygen species) attack the C8 of guanine, resulting in a carbonyl carbon with subsequent protonation at N7 (5). In mammalian cells alone, up to 8.6×10^4 of these adducts occur daily (6,7).

Several crystal structures and molecular dynamics (MD) simulations of polymerases containing oxoG on the templating strand have been reported (8–16). They show that oxoG residues in double-stranded DNA (dsDNA) participate in traditional Watson-Crick hydrogen bonding when opposite cytosine. However, due to steric repulsion between the C8 carbonyl and the phosphate backbone of the corresponding oxoguanyl residue, oxoG can rotate 180° and assume a *syn* conformation; this orientation can lead to Hoogsteen basepairing with adenine (17). Not surprisingly, crystal structures with template oxoG show that this adduct is in *anti* conformation when pairing with incoming dCTP (13,18), and assumes a *syn* conformation when opposite to dATP (9,14,19). Due to this dual coding nature, oxoG adducts exhibit high mutagenic potential and may directly contribute to G:C → T:A transversions, a point mutation linked to somatic cancers (20–22).

Extensive kinetic data show that the preference for insertion of dCTP versus dATP opposite oxoG varies greatly. Human DNA polymerase β, the primary repair polymerase in the base excision repair pathway in mammals (23–25), does not exhibit great discrimination between the incorporation of dATP versus dCTP. Crystal structures and MD simulations reveal that pol β does not accommodate the oxidized base well, due to steric hindrance and altered active site geometry. However, computations and experiments have shown that pol β inserts dCTP opposite oxoG slightly better than dATP (11,15,16,26). On the other hand, DNA polymerase λ, another X-family enzyme, readily inserts either dCTP or dATP opposite oxoG as efficiently as native G:C (15,27).

Low-fidelity DNA polymerase X (pol X) is a 174-amino-acid repair polymerase that is homologous to pol β (28–30). Both these X family members are left-handed DNA polymerases. Following traditional nomenclature used to describe the function of subdomains in DNA polymerases, the X family polymerases exhibit finger, palm, and thumb subdomains, oriented from the N-terminus, respectively (31) (Fig. 1). Each subdomain is involved in the catalytic

Submitted June 17, 2013, and accepted for publication October 15, 2013.
*Correspondence: schlick@nyu.edu or bsampoli@mmm.edu
Editor: Michael Feig.

0006-3495/13/12/2559/10 $2.00
http://dx.doi.org/10.1016/j.bpj.2013.10.014

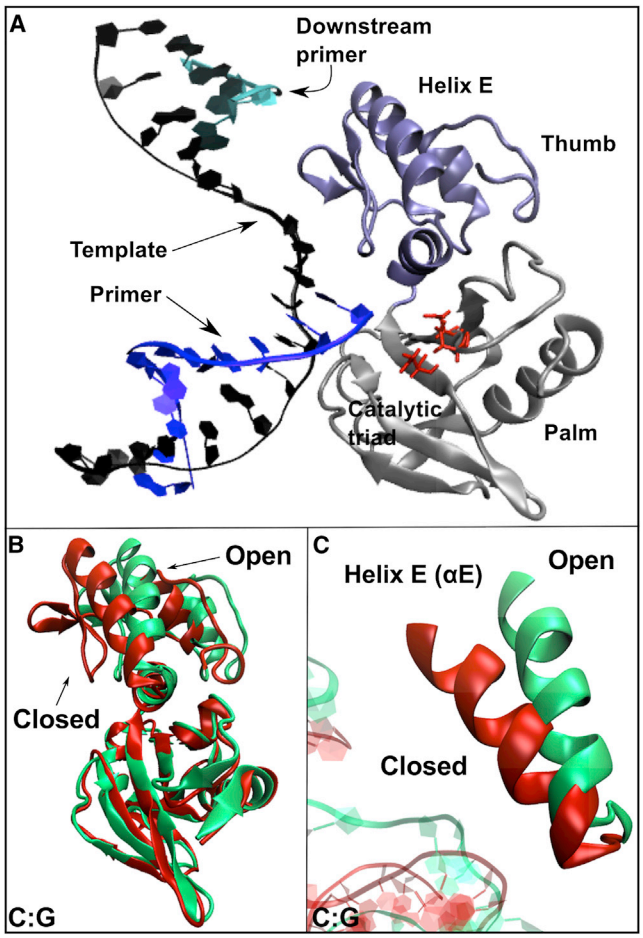

FIGURE 1 Observed motion of αE in pol X in wild-type C:G ternary complex. (*A*) Cartoon representation of open ternary complex of pol X with gapped DNA. The thumb and palm subdomains of pol X are shown in lilac and gray, respectively. The catalytic triad, represented as a stick model, is shown in red. (*B*) Ribbon diagram of pol X with modeled DNA in the initial, open structure (*green*) and final simulated system (*red*). Depicted here is the final simulated structure for C:G from Sampoli Benítez et al. (36). (*C*) Close-up of αE. To see this figure in color, go online.

potential of the polymerase. The finger subdomain is responsible for binding to and stabilizing dsDNA, whereas the thumb is responsible for nascent basepair binding. The palm subdomain coordinates two Mg^{2+} ions via a highly conserved carboxylate triad, and is responsible for nucleotidyl transfer (31,32). Family X members' pol β and pol λ also contain a second N-terminal catalytic domain, which exhibits lyase activity (31,33). Unlike pol β and pol λ, the N-terminal dRP lyase and finger domains of pol X are missing, yielding the smallest known DNA polymerase (30). The thumb and palm morphology of pol X exhibits 55% homology to both the carboxyl terminal thumb and palm subdomains of pol β (29,34). The absence of the finger subdomain renders the active site of pol X solvent exposed, possibly contributing to its low fidelity. Experiments in the Tsai laboratory have shown that pol X exhibits a high tolerance for mismatch pairing and can incorporate a G:G mismatch 35% as efficiently as traditional G:C Watson-Crick basepairs (35) (Table 1). In agreement with experimental data for other polymerases, MD simulations in our lab have shown that pol X exists in two conformations, an open form, not conducive to catalysis, and a closed form where the thumb subdomain closes on the DNA (36,37) (Fig. 1). We have also shown that the closed form is the preferred conformation in the presence of the correct nucleotide and in a G:G mispair (with incoming dGTP in *syn* conformation), in agreement with kinetics studies (35,36).

Extensive kinetic data are also available for pol X's nucleotide incorporation opposite oxoG (38). It is plausible that this oxidative lesion is even more common in viral DNA than in host nuclear DNA. Because African swine fever virus recruits host cell mitochondria to a viral replication site to contend with energy demands, it is not unreasonable to presume that viral DNA polymerases may encounter this common adduct frequently (39,40). The kinetic experiments reveal that, in contrast to pol β and λ, pol X preferentially incorporates dATP opposite oxoG (38) (Table 1). Surprisingly, pol X also facilitates dATP insertion opposite oxoG 1.3 times more efficiently than dCTP opposite G (35,38). Unfortunately, no structural data of DNA/protein complexes are available for pol X. Here, we employ modeling and MD simulations to shed light on the atomistic detail of the protein and DNA interactions. We examine pol X in the presence of gapped DNA with oxoG on the template strand and consider incoming dCTP, dATP, or dGTP units, whereas the templating oxoG assumes either the *anti* or *syn* conformation (Table 2). We also compare the active site geometry, basepairing, and α-helix E (αE) motion of these systems to reported MD data for the pol X/DNA/dCTP ternary complex. Our results provide structural insights into the mechanism by which this polymerase can accommodate incoming nucleotides opposite oxoG and help interpret macroscopic kinetic data for pol X. Namely, we observe that optimal geometry is achieved in the oxoG:A system with oxoG in *syn* conformation. In the oxoG:C system, although the

TABLE 1 Kinetics data for pol X

Basepairing	k_{pol}/K_d (M^{-1} s^{-1})	K_d (μM)	Fidelity[a]
oxoG:C[b]	1000	63	NA
oxoG:G[b]	11	27	92
oxoG:A[b]	2100	56	1.5
G:C[b]	1500	39	NA
G:G[c]	130	21	3.8
G:A[c]	30	20	30

In the basepair notation X:Y, X refers to the templating position and Y denotes the incoming nucleotide.

[a]Fidelity is defined as $[(k_{pol}/K_{d,app})_{cor} + (k_{pol}/K_{d,app})_{inc}]/(k_{pol}/K_{d,app})_{inc}$, where the subscripts cor and inc refer to correct and incorrect nucleotide incorporation, respectively.

[b]From Kumar et al. (38).

[c]From Lamarche et al. (35).

TABLE 2 Summary of MD simulations

System	Total # atoms	Time (ns)	αE closing	Basepairing	Active site geometry	Relative potential Energy (kcal/mol)
G:C[a]	39441	10.5	yes	Watson-Crick	optimal	N/A
oxoG:C	39442	19/30	yes	Watson-Crick	near optimal	182.46
oxoG$_{syn}$:A	39444	19/30	yes	Hoogsteen	optimal	−34.52
oxoG:A$_{syn}$	39444	19	intermediate	staggered	optimal	323.78
oxoG:G	39445	19/30	no	staggered	distorted	310.64
oxoG$_{syn}$:G	39445	19	yes	remote	distorted	284.66

[a]From Sampoli Benitez et al. (37).

thumb subdomain closes, the active site is not in a catalytic-competent geometry. These results provide a missing structural and dynamic picture of preferential nucleotide accommodation opposite an oxidative lesion in pol X, which are in full agreement with available kinetic data.

COMPUTATIONAL METHODOLOGY

Systems setup

The Cartesian coordinates for the five ternary complexes (Table 2), each consisting of African swine fever virus pol X, a 16-mer double-stranded gapped DNA, and an incoming dNTP, were built using INSIGHT II Biopolymer module (Accelrys, San Diego, CA). These five systems survey a combination of oxoG *syn* and oxoG *anti* with incoming nucleotide dCTP$_{anti}$, dATP$_{anti}$, dATP$_{syn}$, dGTP$_{anti}$, and dGTP$_{syn}$. We use the previously reported pol X/DNA/dCTP ternary complex as a starting structure (37), which has a guanine on the template strand at the abasic site. The oxidative residue oxoG is generated using CHARMM with parameter files previously optimized for this system (26). The explicit systems contain 11,783 water molecules, two magnesium ions, as well as monovalent counter-ions for electric neutrality at an ionic strength of 150 mM (35 Cl^- and 28 Na^+). We built the oxoG:C ternary structure after converting the template guanine to 8-oxoguanine. Two oxoG:G systems are built by substituting dCTP for dGTP in an *anti* conformation. In one of the oxoG:G systems, the template oxoG is rotated 180° with respect to the deoxyribose moiety into a *syn* conformation (oxoG$_{syn}$:G). The *syn* conformation is obtained by changing the value of the X dihedral angle to +90° using the Builder module of the INSIGHT II software package (Accelrys). We model two oxoG:A systems with dATP as the incoming nucleotide, and we explore both the *anti* and *syn*. The five resulting models are studied using dynamics simulations (Table 2).

Simulation protocol

All models are energy-minimized and equilibrated using NAMD, and MD simulations are performed using NAMD (41,42) with the CHARMM27 force field (43). Each model is minimized for 1000 steps and then equilibrated for 20 ps using an isothermal-isobaric (NPT) ensemble at 300 K. In the first minimization/equilibration all heavy atoms of the protein are fixed to allow for the relaxation of only the water molecules. A second minimization is then run with all mobile atoms using a canonical (NVT) ensemble for 5000 steps at 300 K, and equilibrated thereafter for 20 ps. Before starting the dynamics production, all systems are evaluated (by plotting the energies, temperatures, and pressures) during the equilibration step to ensure each system's stability. The SHAKE algorithm (44) is employed to constrain the bonds involving hydrogen atoms in the oxoG$_{syn}$:A system. The pressure is maintained at 1 atm using a Langevin piston Nosé-Hoover barostat with an oscillation period of 200 fs and a decay time of 100 fs. Each system is simulated in periodic boundary conditions, with full electrostatics calculated using the particle mesh Ewald method (45,46) with grid spacing $\leq$1 Å. Short-range nonbonded interactions are evaluated at every step using a 12 Å cutoff for van der Waals contacts and a smooth switching function. All simulations are run for at least 20–30 ns. For comparison, we also ran a simulation of pol X/gapped DNA without incoming nucleotide (referred to as the binary system) for 20 ns using the same simulation protocol described previously. The simulations for three systems critical to our results were repeated (oxoG:C, oxoG:G, and oxoG$_{syn}$:A). In these new simulations, the structures are reequilibrated for 200 ps before dynamics production of 30 ns. All other parameters are kept as above.

The potential energies for each system are extracted using the NAMDenergy plugin through Visual Molecular Dynamics. The potential energies for the last nanosecond of each 19 ns trajectory are averaged and presented in Table 2.

RESULTS

Pol X undergoes large subdomain motions in most of the systems studied

Our previous studies have shown that αE closing is critical for active site assembly. Here, we observe large-scale protein motions in all systems (Table 2), with the exception of oxoG:G and the binary complex. A superimposition of the final simulated structures—obtained by averaging the last ns in the dynamics trajectory—reveals that this motion is

concentrated on αE (residues 120–132) (Fig. 2). When comparing the oxoG$_{syn}$:A and oxoG:C systems, it is evident that there are different modes of closing (Fig. 2 *B*). To analyze these motions, we compare our systems to reference open and closed states. More specifically, by open we mean the initial open structure of pol X in the ternary C:G complex, and by closed we mean the simulated final structure of the pol X C:G structure. We chose this system as a reference because it exhibits the largest αE motion (36) (see also Fig. 1). The time evolution of root mean-square deviation (RMSD) of αE relative to the palm subdomain (residues 1 to 105) of open and closed structures is shown in Fig. 3. For the systems for which we have repeated trajectories (namely oxoG:C, oxoG:G, and oxoG$_{syn}$:A), the plots show the average RMSD values obtained for the two runs. For comparison, we also report the data for the binary complex. Upon inspection of these plots, we observe that αE approaches the closed state in 4 out of 6 simulations (oxoG$_{syn}$:A, oxoG:C, oxoG$_{syn}$:G, and oxoG:A$_{syn}$) (Fig. 3). In contrast, αE of oxoGG samples conformations in an intermediate state, and αE of the binary system appears to sample conformations closer to the open state. The RMSD for oxoG$_{syn}$:A superimposed to the open structure appears to fluctuate more than the corresponding RMSD superimposed on the closed structure. This is because αE in this system closes even more than in the reference closed structure, resulting in higher RMSD values when superimposed with respect to the open structure, and smaller RMSD values when superimposed with respect to the closed structure (Fig. S1 in the Supporting Material).

Careful inspection of αE movement reveals that the helix undergoes segmented motion. Therefore, this motion is best described by separately plotting the RMSD of the N- and C-terminal segments of αE with respect to the open structure, where the N- and C-terminal are defined

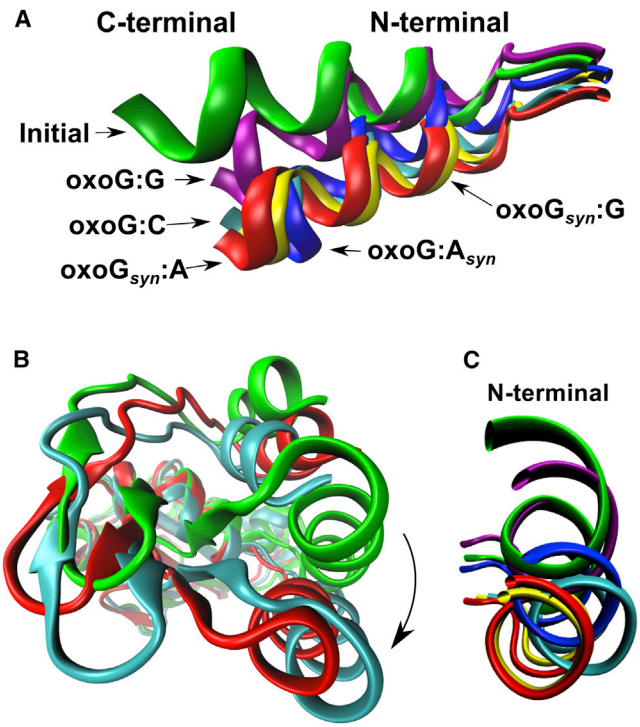

FIGURE 2 Pol X preference for the closed conformation. (*A*) Evidence of αE closing in our simulated systems: oxoG$_{syn}$:A (*red*), oxoG:A$_{syn}$ (*blue*), oxoG:G (*purple*), oxoG:C (*cyan*), oxoG$_{syn}$:G (*yellow*). The calculated average structures over the last ns of simulation are shown. The initial open structure is green. For clarity, residues on αE (120–132) and two adjacent residues (118 and 119) before the helix are shown (118–132 in total). (*B*) Thumb movement observed in open and closed structures. Shown here are final simulated oxoG$_{syn}$:A (*red*), oxoG:C (*cyan*) structures, and the initial open ternary structure (*green*). Both final simulated structures exhibit a closed conformation, but they vary considerably in their final positions. (*C*) Rendering of the average position of the N-terminal segment of αE (residues 120–126) during the last ns of the simulation with color coding as in panel *A*. To see this figure in color, go online.

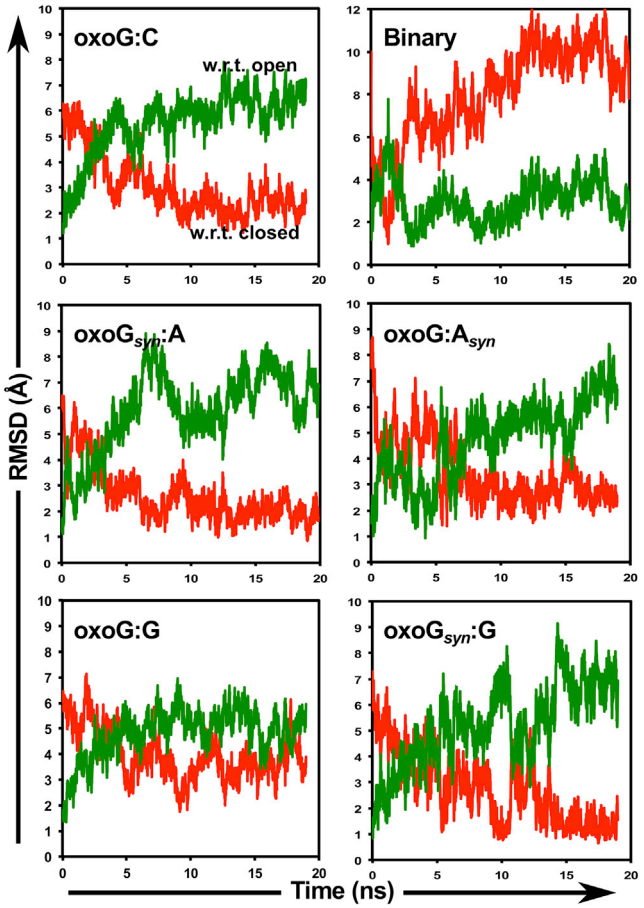

FIGURE 3 Overall αE motions of oxoG/Pol X systems. Time evolution of the RMSD of αE (residues 120 to 132) superimposed to the closed (*red*) and the open (*green*) structures. The three plots on the left (oxoG:C, oxoG$_{syn}$:A, and oxoG:G) represent averaged data collected from duplicate simulations. These data were generated using the Visual Molecular Dynamics RMSD trajectory tool aligning the palm subdomain (1–105) of the closed and open structures of the previously analyzed C:G system. The *y* axis represents RMSD in Å and the *x* axis represents time (ns). To see this figure in color, go online.

as residues 120–126 and 127–132, respectively (Fig. S2). We find that in some cases, the motion of the helix is concentrated on the tip or C-terminal portion (e.g., in oxoG:A_{syn} and oxoG:G), whereas in other cases (e.g., in oxoG:C and oxoG_{syn}:A), both C- and N-terminal portions of the helix move together. Motions of the C-terminal segment appear to be driven primarily by electrostatic interactions between positively charged residues at the C-terminal end of αE (Lys^{131} and Lys^{132}) and the phosphate backbone of the downstream DNA. We hypothesize that these interactions are associated with the dsDNA binding. This suggestion is supported by previous kinetic experiments, which show that pol X binds gapped DNA with considerable cooperative interactions, particularly with decreasing gap size (47,48). In addition, the role of αE in binding to single-stranded and double-stranded DNA has been suggested by extensive stop-flow kinetics and fluorescent titrations experiments (47–51). Furthermore, this hypothesis is supported by NMR experiments: ^{15}N-HSQC spectra of pol X with increasing concentrations of gapped DNA show significant chemical shift perturbations, especially for residues on the C-terminal segment of αE, suggesting its involvement in binding to dsDNA (52).

The N-terminal segment of αE is important for reaction-competent geometry

Motions of the N-terminal segment of αE appear to be correlated with the nature of the incoming nucleotide in the binding pocket. Therefore, we focus on this portion, because it exhibits a nucleotide-dependent motion that can shed light on the mechanism of nucleotide discrimination. From here on, in discussing the αE motion we refer to the N-terminal segment of αE. Using this definition, we can see that, in the oxoG:C, oxoG_{syn}:A, and oxoG_{syn}:G simulated structures, αE closes. In contrast, the protein remains open in the oxoG:G system, whereas it reaches an intermediate state in the oxoG:A_{syn} system (Fig. 2 *C*).

Residues in the N-terminal segment, namely Val^{120} and Ile^{124}, may help stabilize the incoming nucleotide and template base, respectively (Fig. 4). Earlier investigations of C:G and G:G_{syn} pol X systems had also implicated the involvement of Ile^{124} and Val^{120} in stabilizing the template base and incoming nucleotide (36,37). Clearly, when van der Waals contacts are made between these residues and the nascent basepair (as in the oxoG_{syn}:A system), optimal active-site geometry—defined as distances in the active site that are conducive to the chemical step—is achieved (Fig. 4). In the oxoG:A_{syn} and oxoG:C systems, Ile^{124} does not appear to be involved in stabilizing the nascent basepair; rather Arg^{127} stacks with oxoG, and Leu^{123} stabilizes the incoming dCTP, interactions not observed in the cognate G:C system. This might explain why αE does not fully close in the oxoG:A_{syn} system, whereas it achieves an alternate closed state in the oxoG:C system.

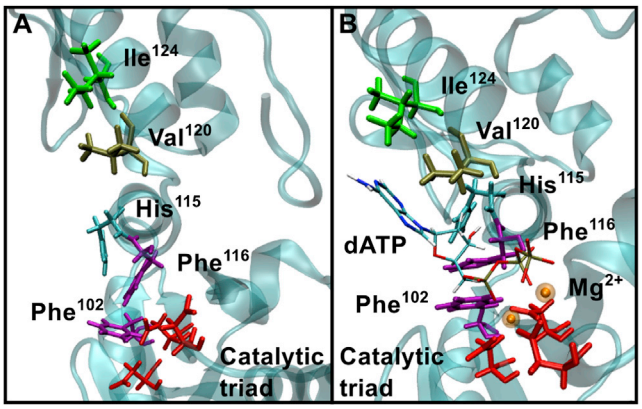

FIGURE 4 Key residues for achieving a catalytic competent state. (*A*) Active site of binary complex reveals little active site organization. Residues important for αE closing are represented as solid colored stick models. (*B*) Active site organization for the simulated oxoG_{syn}:A system. The two Mg^{2+} ions and the incoming dATP are also shown. Full αE closure is observed here, where residues Ile^{124} (*green*) and Val^{120} (*brown*) appear to form van der Waals contacts with the template base oxoG (*gray*) and the incoming nucleotide (*magenta*), respectively. Residues involved with the closing of pol X are also represented by solid stick models, and reveal optimal active site rearrangements. To see this figure in color, go online.

Other local side-chain motions are associated with the open/closed transitions

Opening/closing transitions of αE are associated with concomitant side-chain motions of residues located not only on αE, but also near the binding pocket (we refer to them as hinge residues) (Fig. 4). Our prior studies of pol X with the correct incoming dNTP highlighted Phe^{102}, Phe^{116}, and His^{115} as critical residues for initiating and stabilizing the closed conformation (37). Here, we observe that Phe^{102} rotates along its Hα-Cα-Cβ-Cγ dihedral angle to initiate thumb closing in all oxoG trajectories, in agreement with previous simulations (37). Analogously, Phe^{116} stacks with Phe^{102} to engage in potential π bond interactions, which may aid in stabilizing the pol X's closed conformation in most systems under study (Fig. 4). Residue His^{115} also appears to be important for stabilizing the incoming nucleotide during closing. Indeed, it forms a water-bridged hydrogen bond with the O3′ of the incoming dNTP in all of the oxoG systems, as well as in the previously reported G:C and G:G_{syn} systems (36). However, in the oxoG:A_{syn}, oxoG_{syn}:G, and oxoG:G systems, this hydrogen bond ruptures during the course of the simulations, because His^{115} either flips or moves away. Interestingly, His^{115} is homologous to Tyr^{271} in pol β. Both MD simulations and crystallographic data of oxoG:A complexes have shown that Tyr^{271} interacts unfavorably with both oxoG and dATP (15), possibly explaining why pol β does not exhibit a preference for incorporating incoming dATP.

Pol X achieves stable basepairing and active site geometry in only a few systems

Stable basepairing is only observed in the oxoG:C and oxoG$_{syn}$:A systems (Fig. 5). In the oxoG:A$_{syn}$ and oxoG:G systems, the basepairs are staggered and in the oxoG$_{syn}$:G system the incoming nucleotide is far from the gapped DNA. In the oxoG:A$_{syn}$ system, the template oxoG extrudes from the active site, hampering optimal hydrogen bonding with the incoming dATP (Fig. S3). Moreover, the incoming dATP rotates over its glycosidic dihedral to accommodate the new conformation of the oxoG (Fig. S3).

Table 3 reports the active site geometry distances for all our oxoG systems and for the pol X reference G:C system (37). This set of distances has been reported to be critical for phosphoryl transfer and should all be below 4 Å for the chemical reaction to proceed (53–55). As shown in Table 3, the nucleotidyl transfer distance approaches values conducive for catalysis only in the oxoG$_{syn}$:A and oxoG:A$_{syn}$ systems. In all structures, the phosphate moiety of the incoming dNTP is stabilized by two Mg^{2+} ions (Fig. 6). All three aspartate residues (Asp^{49}, Asp^{51}, and Asp^{100}) interact with two Mg^{2+} ions and the triphosphate moiety of the incoming dNTP in the oxoG$_{syn}$:A, oxoG:G, and oxoG:A$_{syn}$ systems. In contrast, only Asp^{49} and Asp^{51} coordinate with the Mg^{2+} ions in the oxoG:C and oxoG$_{syn}$:G systems (Fig. 6). In both of these trajectories, two water molecules coordinate with the catalytic Mg^{2+} instead. Overall, only oxoG$_{syn}$:A exhibits both optimal active site geometry and stable basepairing. The oxoG:C system exhibits traditional Watson-Crick basepairing, but the catalytic distances between Pα-O3′are suboptimal (Table 3).

In summary, our results show that large subdomain motions (e.g., αE closing,) are necessary to stabilize the incoming nucleotide. Indeed, αE closing is achieved in the oxoG$_{syn}$:A and oxoG:C systems where basepairing is stable. In the case of oxoG$_{syn}$:G, we observe αE closing, but not basepairing because the DNA moves away from the protein and the templating base is >10 Å away from the incoming nucleotide. On the other hand, in systems where αE mostly samples intermediate or open-like conformations (such as oxoG:G and oxoG:A$_{syn}$), good basepairing between the incoming nucleotide and the template base is not observed. This trend is also reflected in the calculated potential energies (protein only) for each system relative to the correct G:C system (Table 1): the extent of αE closing is correlated with the lower energies. For the oxoG$_{syn}$:A system, the potential energy is even lower than for the correct G:C system, signaling formation of a more tightly closed complex in the former. This result agrees with the published kinetic data that show higher incorporation rates for the oxoG:A mismatch than for the correct Watson-Crick (G:C) system (Table 1). Interestingly, our results show that, in addition to stabilizing interaction of αE, further induced-fit side-chain motions that occur upon binding the incoming nucleotide are also required to attain a reaction-competent state. As shown in Tables 2 and 3, optimal active site geometry is only observed in two of the examined systems, oxoG$_{syn}$:A and oxoG:A$_{syn}$, whereas near-optimal geometry (some distances within and others larger than the values for the

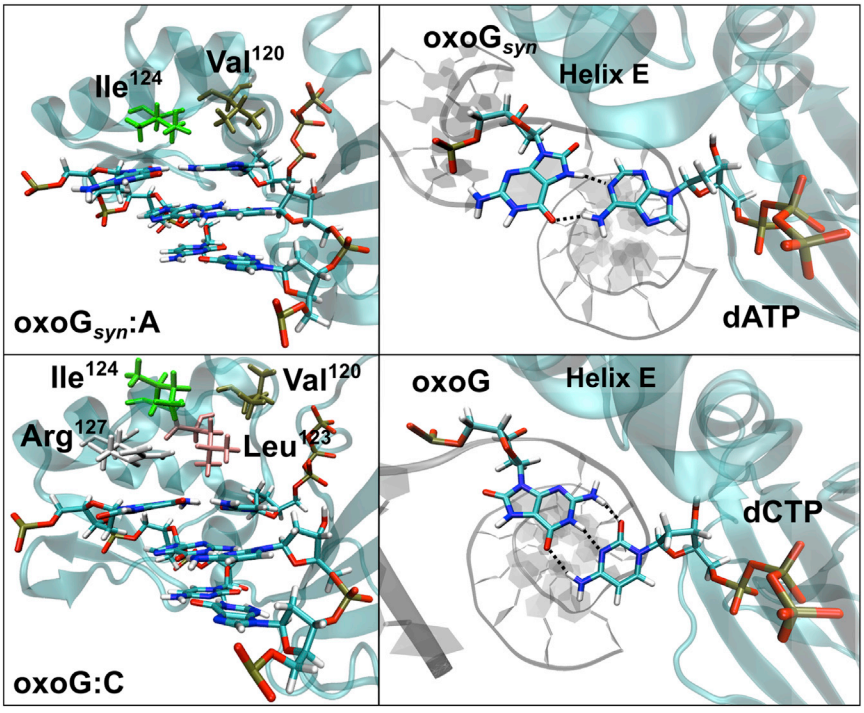

FIGURE 5 Comparison of basepairing in oxoG$_{syn}$:A and oxoG:C systems. In the oxoG$_{syn}$:A system (*upper panels*) the Hoogsteen face of oxoG$_{syn}$ forms stable contacts with the incoming nucleotide dATP. Traditional Watson-Crick basepairing is observed in the oxoG:C system between template oxoG$_{anti}$ and incoming dCTP$_{anti}$ (*lower panels*). To see this figure in color, go online.

TABLE 3 Average active-site interatomic distances for simulated oxoG systems and G:C system

			Distance (Å)			
	G:C[6]	oxoG$_{syn}$:A	oxoG:A$_{syn}$	oxoG:C	oxoG:G	oxoG$_{syn}$:G
Catalytic magnesium ion coordination						
dNTP(P)-P10 (O3′)	5.43	3.82	3.56	7.24	6.13	15.54
Mg^{2+} - P10 (O3′)	5.01	5.25	5.14	7.98	8.52	18.04
Mg^{2+} -dNTP (O1α)	1.84	1.79	1.81	1.83	1.85	1.8
Nucleotide-binding magnesium ion coordination						
Mg^{2+} -dNTP (O1α)	4.3	4.24	4.22	4.27	5.51	4.19
Mg^{2+} -dNTP (O2γ)	1.91	1.91	1.87	1.92	4.27	1.94

correct system) is observed in the oxoG:C system. However, oxoG:A$_{syn}$ exhibits poor baseparing and samples intermediate or open-like conformations. Similarly, the oxoG:G system, whose αE does not close, exhibits the worst active site geometry. Thus, only oxoG$_{syn}$:A exhibits a tightly closed conformation, excellent basepairing, and active site geometry conducive for chemistry.

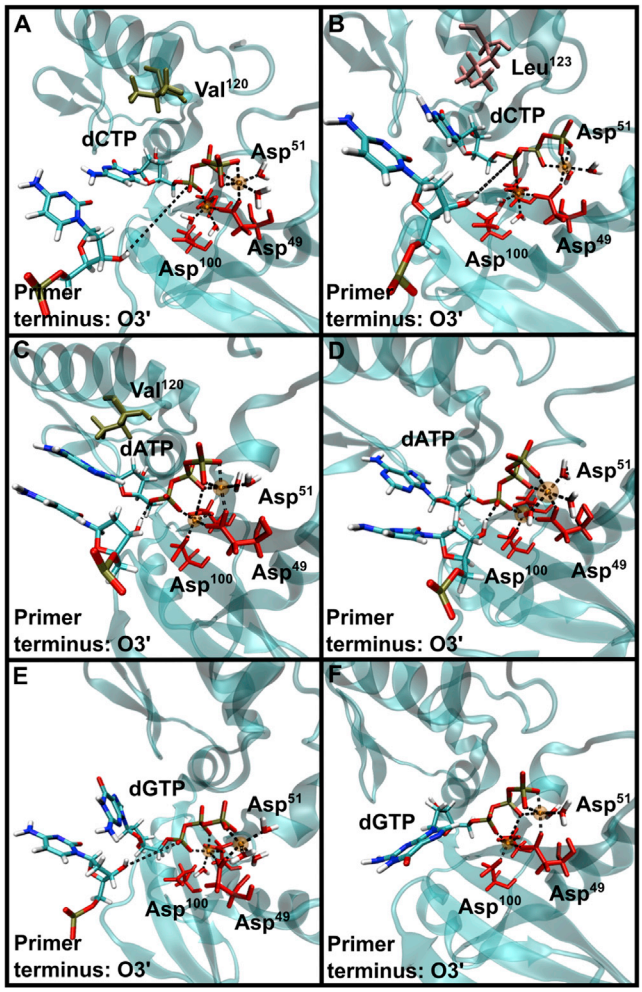

FIGURE 6 Active site geometries of the oxoG/pol X systems. Shown are geometries for systems (*A*) G:C, (*B*) oxoG:C, (*C*) oxoG$_{syn}$:A, (*D*) oxoG:A$_{syn}$ (*E*) oxoG:G, and (*F*) oxoG$_{syn}$:G. In panels *A*, *B*, and *E*, the catalytic Mg^{2+} is not coordinated with Asp^{100}. In panel *F* the O3′ primer terminus is too far from the active site to be included. Residues important for stabilizing the incoming dNTP are shown in colored stick models. Panels *A* and *C* highlight involvement of Val^{120}. Panel *B* reveals the alternative involvement of Leu^{123} in stabilizing the incoming dNTP (residues within 3 Å are shown). To see this figure in color, go online.

DISCUSSION

Kinetic studies on pol X have shown that it preferentially incorporates dATP opposite oxoG. However, this result is in contrast to other X family polymerases that have been thoroughly characterized via both kinetic and structural investigations (4,15,16,26,27,56,57). What, then, is the underlying structural reason for this surprising result from kinetic studies? Our data suggest two possible reasons for this behavior.

First, our results show that residues on αE help stabilize the incoming nucleotide and form particularly favorable interactions when the incoming nucleotide is dATP. Second, the open active site does not constrain the dsDNA as in other systems, allowing oxoG to freely rotate, achieving the more favorable *syn* conformation when opposite dATP. In fact, our data reveal that the incoming dATP is only accommodated when oxoG assumes a *syn* conformation, as reported in several other DNA polymerases crystal structures (9,12,26).

In comparison, in pol β, residues on helix N stabilize the incoming dCTP and dATP, in a similar fashion and therefore do not discriminate between the two. Interestingly, Val^{120} is analogous to Asp^{276} on αN of pol β (Table 4). Asp^{276} has been directly implicated in stabilizing the incoming dNTP (58) and mutant analysis for pol β reveals that when Asp^{276} is substituted for valine, binding affinity for the incoming dNTP increases ninefold (59). This same study reveals an overall decrease in fidelity for pol β. The additional presence of a methyl group in valine may increase the van der Waals interactions with the incoming nucleotide explaining this tighter binding. At the same time, this interaction might be more substantial with a purine base (dATP) than with a pyrimidine (dCTP), explaining why pol X, which has a valine in that position, exhibits a preference for the former. Moreover, these data also suggest a role for Val^{120} in accounting for the low fidelity observed for pol X. These detailed structural insights from simulations

TABLE 4 Key residues around active site, analogous residues in X family members, and proposed functions

pol X	pol β	pol λ	Function in pol X	Function in other polymerases
Asp^{49}	Asp^{190}	Asp^{427}	Coordinates with Mg^{2+} for chemical reaction	Coordinates with Mg^{2+} for chemical reaction
Asp^{51}	Asp^{192}	Asp^{429}	Coordinates with Mg^{2+} for chemical reaction	Coordinates with Mg^{2+} for chemical reaction
Asp^{100}	Asp^{256}	Asp^{490}	Coordinates with Mg^{2+} for chemical reaction	Coordinates with Mg^{2+} for chemical reaction
Phe^{116}	Phe^{272}	Phe^{506}	Interacts with key residues to stabilize conformational change	Flips to initiate thumb subdomain motion
Phe^{102}	Arg^{258}	Ile^{492}	Flips to initiate thumb subdomain motion	Interacts with key residues to stabilize conformational change
Val^{120}	Asp^{276}	Ala^{510}	Accommodates the incoming dNTP	Weakens binding affinity with the nucleotide (pol β)
Ile^{124}	Lys^{280}	Arg^{514}	Stacks with template base in closed state	Responds to thumb motion (pol λ) and stacks with template base in closed state
His^{115}	Tyr^{271}	Tyr^{505}	Accommodates the incoming dNTP through water	Contacts DNA bases
Lys^{131}	Leu^{287}		Interacts with dsDNA downstream the insertion site	
Lys^{132}	Glu^{288}		Interacts with dsDNA downstream the insertion site	

Data adapted from Foley et al. (55) and Sampoli Benitez et al. (37).

help explain the observed experimental kinetic data showing that pol X facilitates the nucleotidyl transfer of A opposite oxoG with greater efficiency than C opposite oxoG, as well as C opposite nondamaged G (38). A recent study on family X DNA polymerase μ shows that the analogous residue Gln^{440} (analogous to pol X Val^{120}) acts as a gatekeeper and helps discriminate between the correct-versus-incorrect incoming nucleotide, further confirming the involvement of this residue in stabilizing the nascent basepair (60).

In recent years there has been growing interest in understanding the role of conformational changes involving enzyme-substrate interactions in catalysis (61). Initial studies on mechanisms of DNA polymerases have suggested an induced fit mechanism, by which the enzyme assumes the correct, catalytically active conformation upon binding to DNA and the correct incoming nucleotide (62). Recent studies have suggested a more nuanced view of DNA polymerase action, in which conformational dynamics are essential to understand the mechanism by which the enzyme binds its ligand(s) (63). According to this conformational sampling theory, the free protein samples an ensemble of different conformations, where it assumes the lowest energy conformation when the right ligand(s) are present. Consequently, the ensemble undergoes a population shift toward the binding conformation (16,64–66). This view has been applied successfully to a number of protein/protein and protein/DNA systems (27,63,65,67). Here, all-atom simulations of ternary complexes of pol X/DNA/dNTP show that pol X samples mostly closed conformations, when active site geometry and/or basepairing are near optimal. In contrast, pol X assumes open or intermediate states when active geometry and basepairing are distorted. In the absence of an incoming nucleotide, pol X samples conformations near to the open state (Fig. 3).

In the presence of correct and incorrect substrates αE adopts nucleotide-dependent conformation states and the movement of the N-terminal segment of αE (residues 120–126) is involved in stabilizing the nascent basepair. However, the closed conformation of αE is not necessarily associated with the well-aligned active site geometry ready for chemistry. Clearly, optimal active site geometry is only observed in three of the examined systems and not observed in the open ternary system for oxoG:G or in our previously published mismatched pair pol X C:C (36). Our data suggest that further induced-fit side-chain motions that occur upon binding the incoming nucleotide are required to attain the reaction-competent state. These observations for pol X are consistent with the hybrid model of substrate binding in which both large-scale thumb rearrangements of the apoenzyme and local reorganization of side chains upon binding correct ligand are important for achieving the proper assembly that leads to catalysis. This hybrid model has explained other biomolecular complexes and interactions (63,65,68,69). Our results suggest that when an incoming nucleotide is present, pol X exhibits conformational flexibility involving αE motion.

CONCLUSIONS

Our dynamics simulations of several oxoG:A, oxoG:C, oxoG:G systems in *syn* and *anti* combinations offer an explanation for the kinetics data observed for pol X. The dynamic fluctuations and energies indicate that pol X achieves optimal active site geometry opposite oxoG with dATP as the incoming nucleotide only when oxoG is in the *syn* (and not *anti*) conformation. We find also that αE of pol X samples closed conformations in 4 out of 6 systems, when including the binary system. However, optimal active site geometry is only achieved in three systems. Based on these data, large-scale movement of αE is necessary, but not sufficient to achieve a reaction competent state. We have uncovered two parts of αE, one of which is involved in dsDNA binding (C-terminus) and the other (N-terminus) involved in stabilizing the incoming nucleotide. In particular, our data provide evidence that optimal active site geometry may be related to key residues of αE, which help stabilize basepairing. In the absence of experimental structural data, our simulations offer an interpretation of the kinetics results.

SUPPORTING MATERIAL

Three figures are available at http://www.biophysj.org/biophysj/supplemental/S0006-3495(13)01145-4.

We thank Shereef Elmetwaly for technical assistance to run the simulations.

This research was supported in part by the Rose M. Badgeley Charitable Trust to Z.R.B. and J.B. and in part by Philip Morris USA Inc. and Philip Morris International and by National Science Foundation (NSF) award MCB-0316771 and National Institutes of Health (NIH) award RO1 E5012692 to T.S.

Finally, we thank the reviewers for their helpful comments.

REFERENCES

1. Beckman, K. B., and B. N. Ames. 1997. Oxidative decay of DNA. *J. Biol. Chem.* 272:19633–19636.
2. Cadet, J., M. Berger, …, S. Spinelli. 1997. Effects of UV and visible radiation on DNA-final base damage. *Biol. Chem.* 378:1275–1286.
3. Cooke, M. S., M. D. Evans, …, J. Lunec. 2003. Oxidative DNA damage: mechanisms, mutation, and disease. *FASEB J.* 17:1195–1214.
4. Beard, W. A., V. K. Batra, and S. H. Wilson. 2010. DNA polymerase structure-based insight on the mutagenic properties of 8-oxoguanine. *Mutat. Res.* 703:18–23.
5. Culp, S. J., B. P. Cho, …, F. E. Evans. 1989. Structural and conformational analyses of 8-hydroxy-2′-deoxyguanosine. *Chem. Res. Toxicol.* 2:416–422.
6. Fraga, C. G., M. K. Shigenaga, …, B. N. Ames. 1990. Oxidative damage to DNA during aging: 8-hydroxy-2′-deoxyguanosine in rat organ DNA and urine. *Proc. Natl. Acad. Sci. USA.* 87:4533–4537.
7. Lindahl, T. 1993. Instability and decay of the primary structure of DNA. *Nature.* 362:709–715.
8. Irimia, A., R. L. Eoff, …, M. Egli. 2009. Structural and functional elucidation of the mechanism promoting error-prone synthesis by human DNA polymerase kappa opposite the 7,8-dihydro-8-oxo-2′-deoxyguanosine adduct. *J. Biol. Chem.* 284:22467–22480.
9. Brieba, L. G., B. F. Eichman, …, T. Ellenberger. 2004. Structural basis for the dual coding potential of 8-oxoguanosine by a high-fidelity DNA polymerase. *EMBO J.* 23:3452–3461.
10. Beckman, J., M. Wang, …, W. H. Konigsberg. 2010. Substitution of ala for tyr567 in rb69 DNA polymerase allows damp to be inserted opposite 7,8-dihydroxy-8-oxoguanine. *Biochemistry.* 49:8554–8563.
11. Krahn, J. M., W. A. Beard, …, S. H. Wilson. 2003. Structure of DNA polymerase beta with the mutagenic DNA lesion 8-oxodeoxyguanine reveals structural insights into its coding potential. *Structure.* 11:121–127.
12. Venkatramani, R., and R. Radhakrishnan. 2008. Effect of oxidatively damaged DNA on the active site preorganization during nucleotide incorporation in a high fidelity polymerase from *Bacillus stearothermophilus*. *Proteins.* 71:1360–1372.
13. Rechkoblit, O., L. Malinina, …, D. J. Patel. 2009. Impact of conformational heterogeneity of OxoG lesions and their pairing partners on bypass fidelity by Y family polymerases. *Structure.* 17:725–736.
14. Vasquez-Del Carpio, R., T. D. Silverstein, …, A. K. Aggarwal. 2009. Structure of human DNA polymerase kappa inserting dATP opposite an 8-OxoG DNA lesion. *PLoS ONE.* 4:e5766.
15. Wang, Y., S. Reddy, …, T. Schlick. 2007. Differing conformational pathways before and after chemistry for insertion of dATP versus dCTP opposite 8-oxoG in DNA polymerase beta. *Biophys. J.* 92:3063–3070.
16. Batra, V. K., D. D. Shock, …, S. H. Wilson. 2012. Binary complex crystal structure of DNA polymerase β reveals multiple conformations of the templating 8-oxoguanine lesion. *Proc. Natl. Acad. Sci. USA.* 109:113–118.
17. Gannett, P. M., and T. P. Sura. 1993. Base pairing of 8-oxoguanosine and 8-oxo-2'-deoxyguanosine with 2'-deoxyadenosine, 2'-deoxycytosine, 2'-deoxyguanosine, and thymidine. *Chem. Res. Toxico.* 6: 690–700.
18. Zang, H., A. Irimia, …, F. P. Guengerich. 2006. Efficient and high fidelity incorporation of dCTP opposite 7,8-dihydro-8-oxodeoxyguanosine by *Sulfolobus solfataricus* DNA polymerase Dpo4. *J. Biol. Chem.* 281:2358–2372.
19. Patro, J. N., M. Urban, and R. D. Kuchta. 2009. Interaction of human DNA polymerase alpha and DNA polymerase I from *Bacillus stearothermophilus* with hypoxanthine and 8-oxoguanine nucleotides. *Biochemistry.* 48:8271–8278.
20. Beckman, K. B., and B. N. Ames. 1998. The free radical theory of aging matures. *Physiol. Rev.* 78:547–581.
21. Pleasance, E. D., R. K. Cheetham, …, M. R. Stratton. 2010. A comprehensive catalogue of somatic mutations from a human cancer genome. *Nature.* 463:191–196.
22. van Loon, B., E. Markkanen, and U. Hübscher. 2010. Oxygen as a friend and enemy: how to combat the mutational potential of 8-oxoguanine. *DNA Repair (Amst.).* 9:604–616.
23. Sobol, R. W., J. K. Horton, …, S. H. Wilson. 1996. Requirement of mammalian DNA polymerase-beta in base-excision repair. *Nature.* 379:183–186.
24. Wilson, S. H. 1998. Mammalian base excision repair and DNA polymerase beta. *Mutat. Res.* 407:203–215.
25. Sawaya, M. R., R. Prasad, …, H. Pelletier. 1997. Crystal structures of human DNA polymerase beta complexed with gapped and nicked DNA: evidence for an induced fit mechanism. *Biochemistry.* 36:11205–11215.
26. Wang, Y., and T. Schlick. 2007. Distinct energetics and closing pathways for DNA polymerase beta with 8-oxoG template and different incoming nucleotides. *BMC Struct. Biol.* 7:7.
27. Picher, A. J., and L. Blanco. 2007. Human DNA polymerase lambda is a proficient extender of primer ends paired to 7,8-dihydro-8-oxoguanine. *DNA Repair (Amst.).* 6:1749–1756.
28. Maciejewski, M. W., R. Shin, …, G. P. Mullen. 2001. Solution structure of a viral DNA repair polymerase. *Nat. Struct. Biol.* 8:936–941.
29. Showalter, A. K., I. J. Byeon, …, M. D. Tsai. 2001. Solution structure of a viral DNA polymerase X and evidence for a mutagenic function. *Nat. Struct. Biol.* 8:942–946.
30. Oliveros, M., R. J. Yáñez, …, L. Blanco. 1997. Characterization of an African swine fever virus 20-kDa DNA polymerase involved in DNA repair. *J. Biol. Chem.* 272:30899–30910.
31. Beard, W. A., and S. H. Wilson. 2000. Structural design of a eukaryotic DNA repair polymerase: DNA polymerase beta. *Mutat. Res.* 460: 231–244.
32. Yang, L., K. Arora, …, T. Schlick. 2004. Critical role of magnesium ions in DNA polymerase beta's closing and active site assembly. *J. Am. Chem. Soc.* 126:8441–8453.
33. DeRose, E. F., T. W. Kirby, …, R. E. London. 2003. Solution structure of the lyase domain of human DNA polymerase lambda. *Biochemistry.* 42:9564–9574.
34. García-Escudero, R., M. García-Díaz, …, J. Salas. 2003. DNA polymerase X of African swine fever virus: insertion fidelity on gapped DNA substrates and AP lyase activity support a role in base excision repair of viral DNA. *J. Mol. Biol.* 326:1403–1412.
35. Lamarche, B. J., S. Kumar, and M. D. Tsai. 2006. ASFV DNA polymerase X is extremely error-prone under diverse assay conditions and within multiple DNA sequence contexts. *Biochemistry.* 45:14826–14833.
36. Sampoli Benítez, B. A., K. Arora, …, T. Schlick. 2008. Mismatched base-pair simulations for ASFV Pol X/DNA complexes help interpret frequent G*G misincorporation. *J. Mol. Biol.* 384:1086–1097.
37. Sampoli Benítez, B. A., K. Arora, and T. Schlick. 2006. In silico studies of the African swine fever virus DNA polymerase X support an induced-fit mechanism. *Biophys. J.* 90:42–56.

38. Kumar, S., B. J. Lamarche, and M. D. Tsai. 2007. Use of damaged DNA and dNTP substrates by the error-prone DNA polymerase X from African swine fever virus. *Biochemistry.* 46:3814–3825.

39. Rojo, G., M. Chamorro, …, J. Salas. 1998. Migration of mitochondria to viral assembly sites in African swine fever virus-infected cells. *J. Virol.* 72:7583–7588.

40. Castelló, A., A. Quintas, …, Y. Revilla. 2009. Regulation of host translational machinery by African swine fever virus. *PLoS Pathog.* 5:e1000562.

41. Phillips, J. C., R. Braun, …, K. Schulten. 2005. Scalable molecular dynamics with NAMD. *J. Comput. Chem.* 26:1781–1802.

42. Kalé, L., R. Skeel, …, K. Schulten. 1999. NAMD2: greater scalability for parallel molecular dynamics. *J. Comput. Phys.* 151:283–312.

43. MacKerell, A. D. J., B. R. Brooks, …, M. Karplus. 1998. CHARMM: the energy function and its parameterization. *In* Encyclopedia of Computational Chemistry. P. v. R. Schleyer, editor. John Wiley and Sons, New York, NY, pp. 271–277.

44. Ryckaert, J. P., G. Ciccotti, and H. J. C. Berendsen. 1977. Numerical integration of the Cartesian equations of motion of a system with constraints: molecular dynamics of *n*-alkanes. *J. Comput. Phys.* 23: 327–341.

45. Darden, T., D. M. York, and L. G. Pedersen. 1993. Particle mesh Ewald: an N•logN method for Ewald sums in large systems. *J. Chem. Phys.* 98:10089–10092.

46. Norberg, J., and L. Nilsson. 2000. On the truncation of long-range electrostatic interactions in DNA. *Biophys. J.* 79:1537–1553.

47. Jezewska, M. J., P. J. Bujalowski, and W. Bujalowski. 2007. Interactions of the DNA polymerase X from African swine fever virus with gapped DNA substrates. Quantitative analysis of functional structures of the formed complexes. *Biochemistry.* 46:12909–12924.

48. Jezewska, M. J., P. J. Bujalowski, and W. Bujalowski. 2007. Interactions of the DNA polymerase X of African swine fever virus with double-stranded DNA. Functional structure of the complex. *J. Mol. Biol.* 373:75–95.

49. Jezewska, M. J., A. Marcinowicz, …, W. Bujalowski. 2006. DNA polymerase X from African swine fever virus: quantitative analysis of the enzyme-ssDNA interactions and the functional structure of the complex. *J. Mol. Biol.* 356:121–141.

50. Jezewska, M. J., M. R. Szymanski, and W. Bujalowski. 2011. Interactions of the DNA polymerase X from African Swine Fever Virus with the ssDNA. Properties of the total DNA-binding site and the strong DNA-binding subsite. *Biophys. Chem.* 158:26–37.

51. Jezewska, M. J., M. R. Szymanski, and W. Bujalowski. 2011. Kinetic mechanism of the ssDNA recognition by the polymerase X from African Swine Fever Virus. Dynamics and energetics of intermediate formations. *Biophys. Chem.* 158:9–20.

52. Su, M.-I. 2004. NMR structural studies of African Swine Fever Virus DNA Polymerase X complexed with gapped DNA and MgdNTP. *Doctoral Dissertation. Ohio State University.* 1–86.

53. Arora, K., and T. Schlick. 2004. In silico evidence for DNA polymerase-beta's substrate-induced conformational change. *Biophys. J.* 87:3088–3099.

54. Batra, V. K., L. Perera, …, S. H. Wilson. 2013. Amino acid substitution in the active site of DNA polymerase β explains the energy barrier of the nucleotidyl transfer reaction. *J. Am. Chem. Soc.* 135:8078–8088.

55. Foley, M. C., K. Arora, and T. Schlick. 2006. Sequential side-chain residue motions transform the binary into the ternary state of DNA polymerase lambda. *Biophys. J.* 91:3182–3195.

56. Miller, H., R. Prasad, …, A. P. Grollman. 2000. 8-oxodGTP incorporation by DNA polymerase beta is modified by active-site residue Asn279. *Biochemistry.* 39:1029–1033.

57. Markkanen, E., B. Castrec, …, U. Hübscher. 2012. A switch between DNA polymerases δ and λ promotes error-free bypass of 8-oxo-G lesions. *Proc. Natl. Acad. Sci. USA.* 109:20401–20406.

58. Yang, L., W. A. Beard, …, T. Schlick. 2004. Highly organized but pliant active site of DNA polymerase beta: compensatory mechanisms in mutant enzymes revealed by dynamics simulations and energy analyses. *Biophys. J.* 86:3392–3408.

59. Vande Berg, B. J., W. A. Beard, and S. H. Wilson. 2001. DNA structure and aspartate 276 influence nucleotide binding to human DNA polymerase beta. Implication for the identity of the rate-limiting conformational change. *J. Biol. Chem.* 276:3408–3416.

60. Li, Y., and T. Schlick. 2013. ''Gate-keeper'' residues and active-site rearrangements in DNA polymerase μ help discriminate non-cognate nucleotides. *PloS Comp Biol.* 9:e1003074.

61. Schlick, T., K. Arora, W. A. Beard, and S. H. Wilson. 2012. Perspective: pre-chemistry conformational changes in DNA polymerase mechanisms. *Theor. Chem. Acc.* 131:1287–1295.

62. Koshland, D. E. 1994. The key-lock theory and the induced-fit theory. *Angew. Chem. Int. Ed. Engl.* 33:2375–2378.

63. Foley, M. C., K. Arora, and T. Schlick. 2012. Intrinsic motions of DNA polymerases underlie their remarkable specificity and selectivity. *In* Innovations in Biomolecular Modeling and Simulations, *Vol. 2.*. The Royal Society of Chemistry, pp. 81–107.

64. Koshland, Jr., D. E. J., G. Némethy, and D. Filmer. 1966. Comparison of experimental binding data and theoretical models in proteins containing subunits. *Biochemistry.* 5:365–385.

65. Arora, K., and C. L. Brooks, 3rd. 2007. Large-scale allosteric conformational transitions of adenylate kinase appear to involve a population-shift mechanism. *Proc. Natl. Acad. Sci. USA.* 104:18496–18501.

66. Bakan, A., and I. Bahar. 2009. The intrinsic dynamics of enzymes plays a dominant role in determining the structural changes induced upon inhibitor binding. *Proc. Natl. Acad. Sci. USA.* 106:14349–14354.

67. Arora, K., and T. Schlick. 2005. Conformational transition pathway of polymerase beta/DNA upon binding correct incoming substrate. *J. Phys. Chem. B.* 109:5358–5367.

68. Grünberg, R., J. Leckner, and M. Nilges. 2004. Complementarity of structure ensembles in protein-protein binding. *Structure.* 12:2125–2136.

69. Wlodarski, T., and B. Zagrovic. 2009. Conformational selection and induced fit mechanism underlie specificity in noncovalent interactions with ubiquitin. *Proc. Natl. Acad. Sci. USA.* 106:19346–19351.

Supporting material:

Sampoli et al.
How DNA polymerase X preferentially accommodates incoming dATP opposite 8-oxoguanine on the template

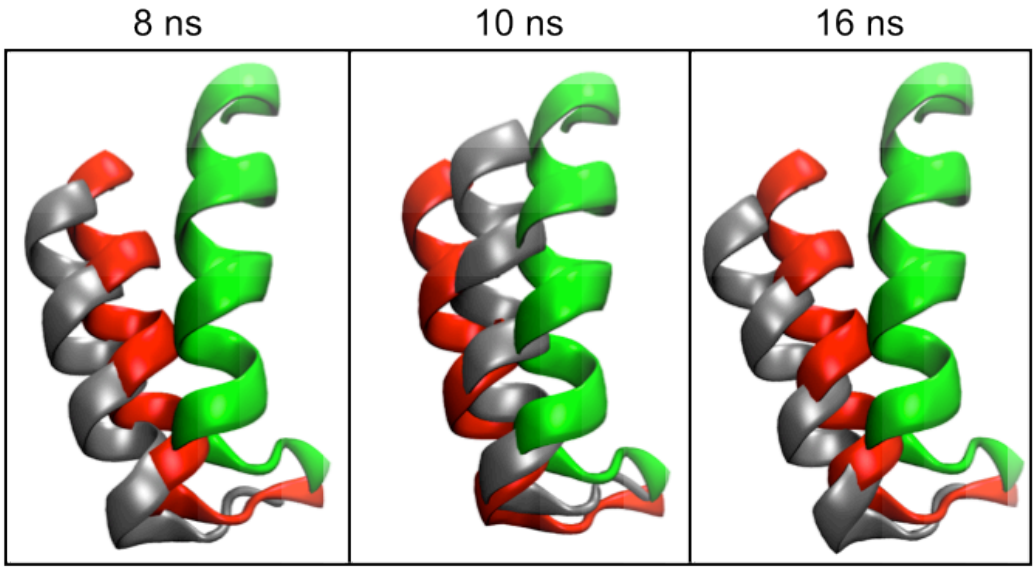

Figure S1. *VMD snapshots of the oxoG$_{syn}$:A system*. Movement of αE in the oxoG$_{syn}$:A system (grey) with respect to the open (green) and closed (red) structures. The panels above show three snapshots taken at different points during the dynamics trajectory While the simulated grey structure oscillates around the closed (red) structure, it appears to deviate significantly from the open (green) structure, giving rise to high RMSD values (See **Figure 3**).

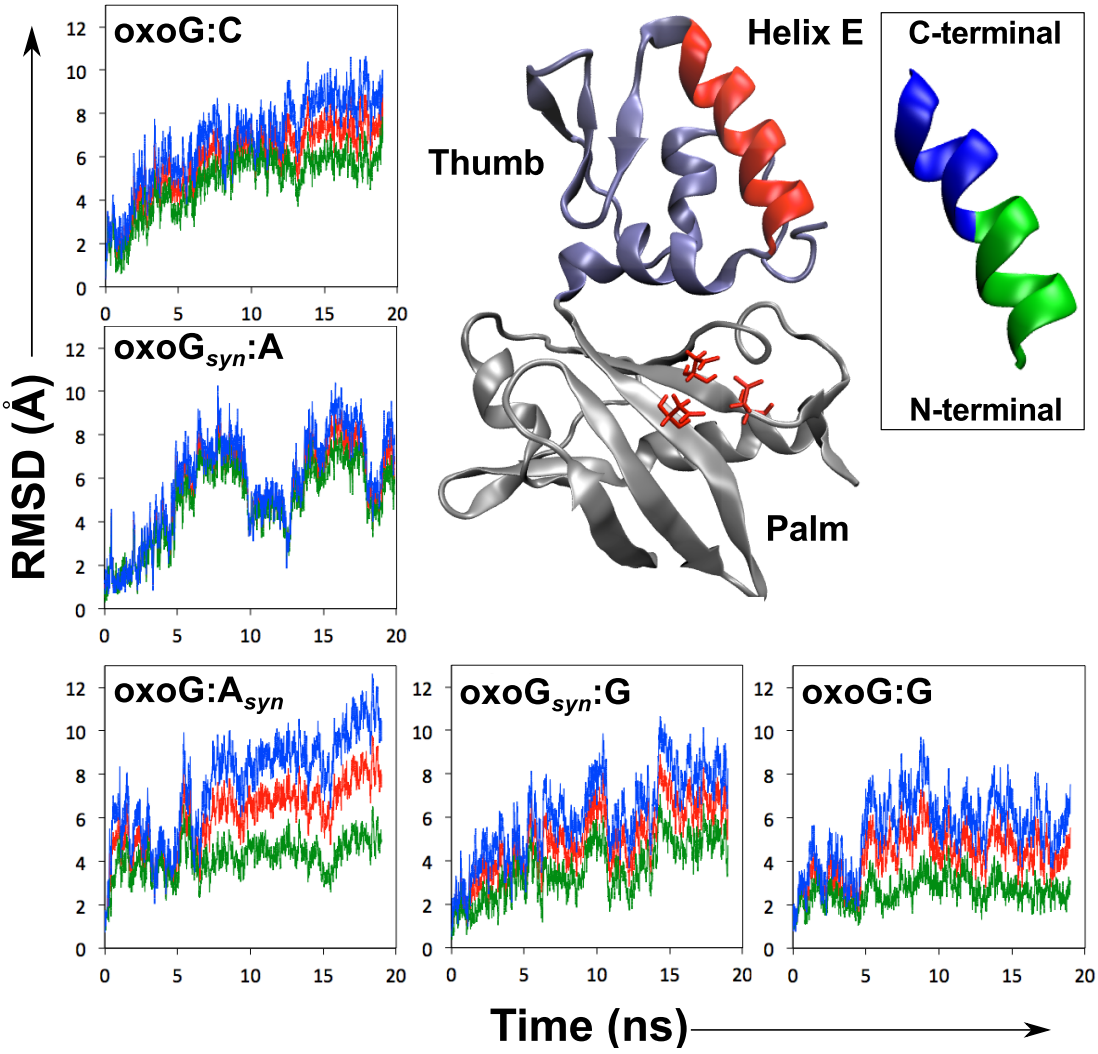

Figure S2. *Segmentation of αE motion in the simulated trajectories.* Time evolution of the root-mean square deviations (RMSD) for αE (red), N-terminal αE segment (120-126) (green) and C-terminal αE segment (127-132) (blue) are shown for all five oxoG systems. These data were generated using VMD RMSD trajectory tool aligning the thumb (107-174) and αE (120-132) to the palm subdomain (1-105) of their initial structures. The y-axis represents RMSD in Å and the x-axis is time (ns). In the top right panel, Pol X is represented as a cartoon model with the palm subdomain (grey), thumb subdomain (purple), and αE (red). The catalytic triad is also displayed as stick-lines in red. The division of αE is magnified, where the N-terminal segment of αE (120-126) is shown in green and the C-terminal segment is in blue.

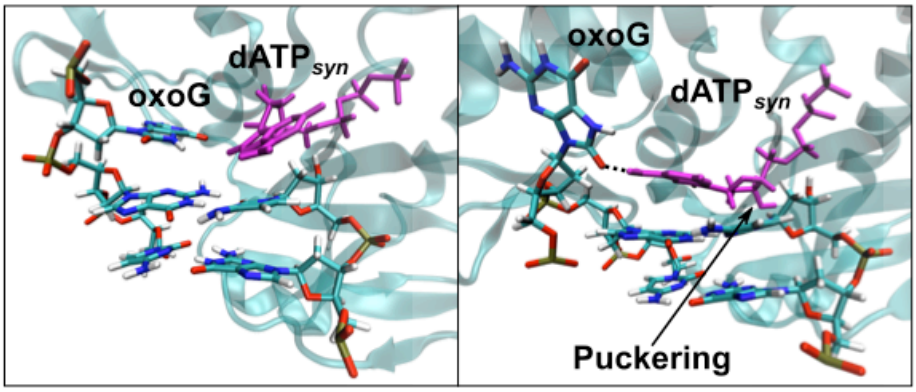

Figure S3: *VMD snapshots of the oxoG:A_{syn} system*. (A) At the beginning of the simulation and (B) after 9 ns, when the incoming dATP (magenta) rotates over its glycosidic dihedral angle. The oxoG on the template strand (gray) also flips towards a *syn* conformation.